

## Supporting Online Material for **Elastic Shear Anisotropy of Ferropericlase in Earth's Lower Mantle**

Hauke Marquardt,\* Sergio Speziale, Hans J. Reichmann, Daniel J. Frost, Frank R. Schilling, Edward J. Garnero

\*To whom correspondence should be addressed. E-mail: hama@gfz-potsdam.de

Published 10 April 2009, *Science* **324**, 224 (2009)  
DOI: 10.1126/science.1169365

### This PDF file includes:

Materials and Methods  
Figs. S1 to S5  
Table S1  
References

## Materials and methods

### *Sample synthesis*

The starting material for the synthesis of ferropericlase single crystals was a fine powdered mixture of reagent grade MgO and Fe<sub>2</sub>O<sub>3</sub>. After drying at 1000°C in a box furnace the powders were mixed under alcohol in the appropriate stoichiometric proportions, then dried in air and compressed into pellets using a 10 mm diameter pellet die. The pellets were sintered in a CO-CO<sub>2</sub> gas-mixing furnace at 1250°C at an oxygen fugacity 2 log units below the fayalite magnetite oxygen buffer. Recovered pellets were ground and then repressed into pellets for re-sintering under identical conditions. After regrinding a powdered sample was loaded into a Fe foil capsule of 1.2mm diameter and 1.3mm long. The capsule was placed at the centre of a 10 mm edge length MgO octahedral pressure assembly that comprised a LaCrO<sub>3</sub> furnace and WRe thermocouple. The assembly was compressed in a 1000 tonne multianvil press using 8 tungsten carbide anvils with 4mm edge length truncations. After pressurising to 24 GPa the sample was heated for 12 hours at 1800°C. The temperature was quenched by turning off the power to the furnace.

The resulting crystals were up to 100µm in size and of excellent optical quality with a light greenish color. Electron microprobe analysis (EMPA) on 12 samples yielded a composition of (Mg<sub>0.900(3)</sub>Fe<sub>0.100(3)</sub>)O and showed that the crystals are chemically homogenous at least on the probing scale of EMPA. The synthesis procedure insured that the Fe<sup>3+</sup>/ΣFe ratio is below the detection limit of Mößbauer Spectroscopy as already documented for ferropericlase synthesised in the same laboratory with the same method (*S1*). X-ray diffraction measurements yielded a lattice constant of 4.229(1)Å and showed no evidence for secondary phases. The lattice parameter is slightly larger than expected from reported data of ferropericlase synthesised at ambient conditions (*S2*), which likely results from the lower Fe<sup>3+</sup>/ΣFe ratio in our samples (*S3*).

### *Brillouin measurements and data analysis*

Brillouin spectroscopy was performed in 60° symmetric forward scattering geometry to 69 GPa in the diamond-anvil cell. Different pressure-transmitting media were used in 3 different experimental runs (table S1), where neon was employed as a pressure-transmitting medium in the highest pressure experiments to ensure a quasi-hydrostatic environment. A typical Brillouin spectrum at 69 GPa is shown in Fig. S1. Shear velocities were measured in the (100) plane at different angles at each pressure (Fig. S2). Brillouin scattering intensity depends on the coupling of the laser light to acoustic phonons in the sample. In our experimental setup, the intensity vanishes for shear waves propagating in (100) plane with polarization in [100]. Data analysis was performed with the raw data which were inverted for the two effective elastic shear constants  $(c_{11}-c_{12})/2$  and  $c_{44}$  (Fig. S3) by using the procedure described in (S4). The density, which is needed to relate measured velocities to elastic moduli, was extracted from Synchrotron x-ray powder diffraction measurements (Fig. S4) performed on the same sample material at the Diamond Light Source, UK. Table S1 shows maximum, minimum and average shear velocity, the effective shear elastic moduli, and the density at each pressure at which Brillouin scattering was performed. Fig. S4 illustrates that the spin-transition of iron is also visible in the x-ray powder diffraction data as reported in previous studies (S5- S7). The results of a previous Brillouin study of MgO (S8) to 55 GPa are not used in this study, because those results are qualitatively inconsistent with other experimental results and the computational data at pressures above ~20GPa, possibly due to wrong assignment of the longitudinal mode, which was measured only in two crystallographic directions and was strongly overlapping with the diamond signal.

#### *Temperature correction in Fig. 4 and extrapolation to (Mg<sub>0.8</sub>Fe<sub>0.2</sub>)O*

To estimate the shear anisotropy of (Mg<sub>0.8</sub>Fe<sub>0.2</sub>)O, we assumed a linear dependence of the shear anisotropy on iron content in (Mg<sub>1-x</sub>Fe<sub>x</sub>)O (for x<0.2) and based the extrapolation on the available data for MgO (*S9, S10*) and our Brillouin data of (Mg<sub>0.9</sub>Fe<sub>0.1</sub>)O.

Temperature correction of the room temperature shear anisotropy of (Mg,Fe)O along a geotherm was performed by using available (computational) high-P/T elasticity data for MgO (*S9*) and assuming that the effect of temperature on shear anisotropy does not differ for (Mg<sub>1-x</sub>Fe<sub>x</sub>)O (for x<0.2). However, it can be seen from Fig. *S5*, that the effect of temperature along a geotherm is less pronounced than the pressure-effect. Furthermore, we assumed that temperature broadens the spin transition region, but does not change the magnitude of anisotropy change. The expected broadening of the spin transition region with temperature was estimated from experimental data on (Mg<sub>0.75</sub>Fe<sub>0.25</sub>)O (*S11*).

#### *Other calculations for Fig. 4*

(a) The model geotherm of Stacey (*S12*) was used to relate depth to temperature. The shear anisotropy of MgO and MgSiO<sub>3</sub> were calculated using available computational data at high pressure and temperature (*S9, S13, S14*). (b) We assumed a lower mantle assemblage (*S15*) that consists of 64 mol% perovskite, 31 mol% ferropericlase (Mg<sub>0.8</sub>Fe<sub>0.2</sub>)O and 5 mol% calcium perovskite. For simplicity, we neglected calcium perovskite in our calculation, we also assumed the perovskite to be MgSiO<sub>3</sub>, disregarding substitution by Fe and Al. Available high pressure and high temperature densities (*S9, S13, S16*) were used to convert the molar fractions into volume fractions along the geotherm. The calculated volume fraction of ferropericlase maintains equal to 20 ± 2% throughout the whole lower mantle.

### *Relationship between our results and of seismic observation in the lower mantle*

The picture emerging from our new results is that ferropericlase is largely more anisotropic than MgO at the pressures of the lower mantle, and it is probably dominating the elastic anisotropy of the lower mantle in all the environments where the deformation of lower mantle rock takes place by dislocation creep (that favours the development of lattice preferred orientation), and the strain level is elevated (*S17*). The apparent absence of seismic anisotropy in large sectors of the lower mantle (as put forth in (*S18*)) might suggest that the bulk lower mantle is dominated by conditions at which deformation is controlled by diffusion creep that does not enhance lattice preferred orientation (*S19, S20*).

However, there are large uncertainties on the depth distribution of seismic anisotropy in the deep lower mantle (*S21*). Clear indications of seismic anisotropy in the lowermost part of the lower mantle have been evident in over two and a half decades of seismic studies, but further up into the lower mantle is difficult to confidently probe, primarily for reasons including (a) a reference seismic phase is usually needed, like SKS to compare a splitting S wave to, or a direct S wave to compare a splitting ScS wave with, (b) need of long seismic paths through a region that has a consistent anisotropy signature, as to generate a measurable effect in the seismic waves, and (c) need of a clear understanding of the lithospheric contribution to the lower mantle phases used to study anisotropy.

Even if the lower mantle above D'' is moderately (or even strongly) anisotropic, and if the mixing and convection scales in the lower mantle are such that the anisotropy signatures are not uniform over significant lateral scales, it is possible that seismic waves cannot properly depict the anisotropy, and it is instead mapped as isotropy.

## Supporting Figures

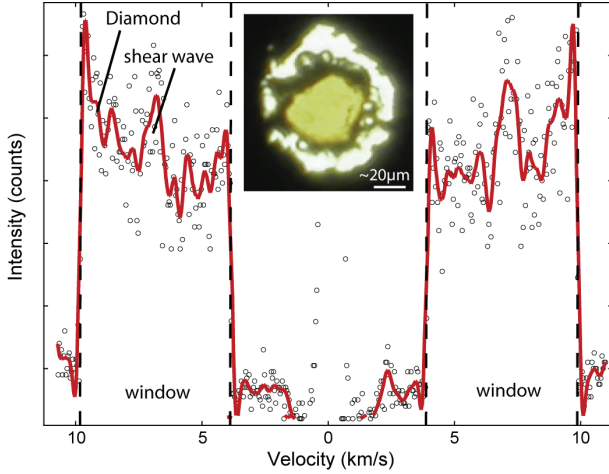


Fig. S1. Brillouin spectrum of  $(\text{Mg}_{0.9}\text{Fe}_{0.1})\text{O}$  at 69 GPa. Shear velocities were measured in the (100) plane at different angles at each pressure and inverted for the two effective elastic shear constants  $(c_{11}-c_{12})/2$  and  $c_{44}$ , which determine the maximum and minimum shear wave propagation velocity. The collection window was set to increase the exposure time in the spectral region of interest (indicated as “window” in the figure). Black circles show raw data, red lines illustrate the data after applying a low-pass filter for noise reduction (only for illustration). Picture shows  $(\text{Mg}_{0.9}\text{Fe}_{0.1})\text{O}$  in the sample chamber with Ne pressure medium and ruby spheres (used as pressure calibrants) at 69 GPa.

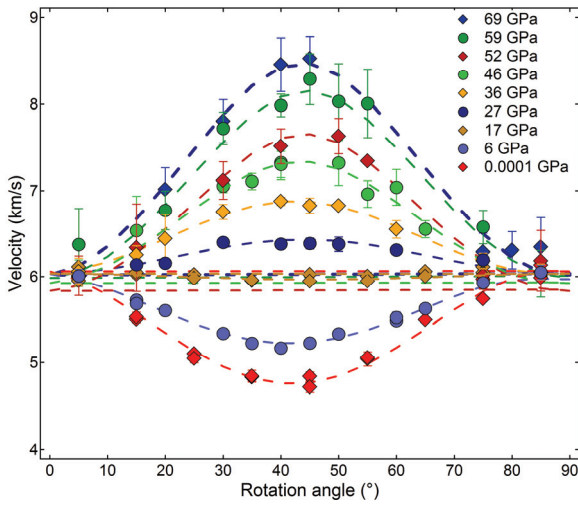


Fig. S2. Measured shear velocities as a function of rotation angle at selected pressures. Velocities were measured over a  $180^\circ$  angular range but can be collapsed to  $90^\circ$  for symmetry reasons. The collecting time per spectrum strongly increased with pressure.

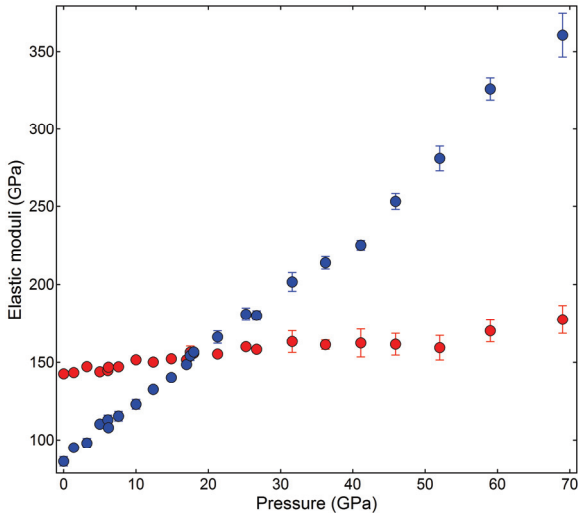


Fig. S3. The two shear moduli  $c_{44}$  (red) and  $(c_{11}-c_{12})/2$  (blue) of  $(\text{Mg}_{0.9}\text{Fe}_{0.1})\text{O}$  as a function of pressure.

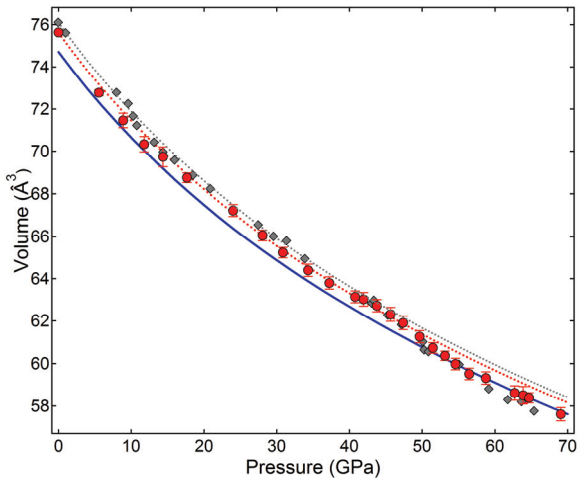


Fig. S4. X-ray powder diffraction data of  $(\text{Mg}_{0.9}\text{Fe}_{0.1})\text{O}$  (red). The spin transition is accompanied by an additional volume decrease with respect to the extrapolation of the HS phase (red dashed line). The compression curves of MgO (blue) (S22) and data for  $(\text{Mg}_{0.83}\text{Fe}_{0.17})\text{O}$  (grey diamonds) (S5) are plotted for comparison.

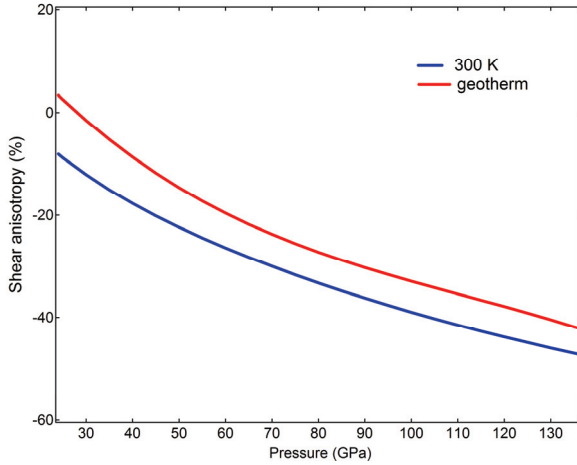


Fig. S5. Shear anisotropy  $(v_{s[001]} - v_{s[011]}) / ((v_{s[001]} + v_{s[011]}) / 2)$  of MgO, calculated along a geotherm (S12) with high P/T computational data (S9), and the shear anisotropy calculated from the same set of computational data at the same pressures at 300 K.

## Supporting Tables

Tab. S1. Pressure ( $P$ ), density, shear moduli  $((c_{11}-c_{12})/2, c_{44}, G_{vrh})$ , shear velocities ( $v_{s[001]}$ ,  $v_{s[011]}$ ,  $v_{s,\text{avg}}$ ), shear anisotropy and employed pressure-transmitting medium (MEW: Methanol-Ethanol-water (16:3:1)). Numbers in brackets are uncertainties in the last given digit and are based on the propagation of the uncertainties in every measured velocity, taking into account the positions of Stokes- and anti-Stokes peaks, their uncertainties and the broadness of the peaks.

| $P$<br>[GPa] | Density<br>[g/cm <sup>3</sup> ] | $(c_{11}-c_{12})/2$<br>[GPa] | $c_{44}$<br>[GPa] | $G_{vrh}$<br>[GPa] | $v_{s[001]}$<br>[km/s] | $v_{s[011]}$<br>[km/s] | $v_{s,\text{avg}}$<br>[km/s] | Shear<br>anisotropy<br>[%] | Pressure<br>Medium |
|--------------|---------------------------------|------------------------------|-------------------|--------------------|------------------------|------------------------|------------------------------|----------------------------|--------------------|
| $10^{-4}$    | 3.82                            | 86(3)                        | 143(2)            | 116(1)             | 6.11(4)                | 4.74(8)                | 5.52(3)                      | 25(2)                      | MEW                |
| 1.4          | 3.85                            | 95(2)                        | 143(2)            | 122(1)             | 6.10(4)                | 4.97(5)                | 5.62(2)                      | 20(1)                      | MEW                |
| 3.2          | 3.89                            | 98(3)                        | 147(2)            | 125(1)             | 6.15(4)                | 5.02(8)                | 5.67(3)                      | 20(2)                      | MEW                |
| 5            | 3.93                            | 110(2)                       | 144(2)            | 129(1)             | 6.05(4)                | 5.29(5)                | 5.73(2)                      | 13(1)                      | Argon              |
| 6.1          | 3.96                            | 113(3)                       | 145(2)            | 131(1)             | 6.05(4)                | 5.34(7)                | 5.75(3)                      | 12(1)                      | Neon               |
| 6.2          | 3.96                            | 108(2)                       | 147(2)            | 130(1)             | 6.09(4)                | 5.22(5)                | 5.72(2)                      | 15(1)                      | MEW                |
| 7.6          | 3.99                            | 115(3)                       | 147(2)            | 133(1)             | 6.07(4)                | 5.37(7)                | 5.78(3)                      | 12(1)                      | MEW                |
| 10           | 4.04                            | 123(3)                       | 152(2)            | 139(1)             | 6.12(4)                | 5.51(7)                | 5.87(3)                      | 11(1)                      | MEW                |
| 12.4         | 4.09                            | 132(2)                       | 150(2)            | 143(1)             | 6.06(4)                | 5.68(4)                | 5.91(2)                      | 6(1)                       | MEW                |
| 14.9         | 4.14                            | 140(2)                       | 152(2)            | 147(1)             | 6.07(4)                | 5.82(4)                | 5.97(2)                      | 4(1)                       | MEW                |
| 17           | 4.18                            | 148(2)                       | 152(2)            | 150(1)             | 6.02(4)                | 5.96(4)                | 6.00(2)                      | 1(1)                       | MEW                |
| 17.5         | 4.19                            | 154(3)                       | 156(4)            | 156(2)             | 6.11(8)                | 6.07(6)                | 6.10(4)                      | 1(2)                       | Argon              |

|      |      |         |        |        |          |          |         |       |       |
|------|------|---------|--------|--------|----------|----------|---------|-------|-------|
| 18   | 4.19 | 157(2)  | 156(2) | 156(1) | 6.09(4)  | 6.11(4)  | 6.10(2) | 0(1)  | Neon  |
| 21.3 | 4.25 | 166(4)  | 155(2) | 159(1) | 6.04(4)  | 6.25(7)  | 6.12(3) | 3(1)  | Argon |
| 25.2 | 4.32 | 181(4)  | 160(2) | 168(1) | 6.08(4)  | 6.47(7)  | 6.24(3) | 6(1)  | Argon |
| 26.7 | 4.35 | 180(3)  | 158(2) | 167(1) | 6.03(4)  | 6.44(5)  | 6.19(2) | 7(1)  | Neon  |
| 31.6 | 4.43 | 202(6)  | 163(7) | 178(4) | 6.07(13) | 6.75(10) | 6.33(6) | 11(3) | Argon |
| 36.2 | 4.50 | 214(4)  | 161(3) | 181(2) | 5.99(6)  | 6.89(6)  | 6.33(3) | 14(1) | Neon  |
| 41.1 | 4.58 | 225(3)  | 162(9) | 185(4) | 5.96(16) | 7.02(5)  | 6.36(8) | 16(3) | Neon  |
| 45.9 | 4.66 | 252(5)  | 161(7) | 193(4) | 5.88(13) | 7.36(7)  | 6.44(6) | 22(2) | Neon  |
| 52   | 4.78 | 282(8)  | 160(8) | 201(5) | 5.78(15) | 7.68(11) | 6.48(7) | 28(3) | Neon  |
| 59   | 4.89 | 326(7)  | 171(7) | 222(4) | 5.91(12) | 8.17(9)  | 6.74(6) | 32(2) | Neon  |
| 69   | 5.01 | 362(14) | 173(9) | 234(6) | 5.88(15) | 8.50(16) | 6.83(9) | 36(3) | Neon  |

## Supporting References

- S1. H. Keppler, I. Kantor, L. Dubrovinsky, *Am. Mineral.* **92**, 433 (2007).
- S2. S. D. Jacobsen *et al.*, *J. Geophys. Res.* **107** (2002).
- S3. C. A. McCammon, J. Peyronneau, J.-P. Poirier, *Geophys. Res. Lett.* **25**, 1589 (1998).
- S4. A. G. Every, *Phys. Rev. B* **22**, 1746 (1980).
- S5. J.-F. Lin *et al.*, *Nature* **436**, 377 (2005).
- S6. S. Speziale *et al.*, *J. Geophys. Res.* **112** (2007).
- S7. Y. Fei *et al.*, *Geophys. Res. Lett.* **34**, L17307 (2007).
- S8. C.-S. Zha, H.-k. Mao, R. J. Hemley, *Proc. Natl. Acad. Sci.* **94**, 13494 (2000).
- S9. B. B. Karki, R. M. Wentzcovitch, S. de Gironcoli, S. Baroni, *Science* **286**, 1705 (1999).
- S10. S. V. Sinogeikin, J. D. Bass, *Phys. Earth Planet. Inter.* **120**, 43 (2000).
- S11. J.-F. Lin *et al.*, *Science* **317**, 1740 (2007).
- S12. F. D. Stacey, *Physics of the Earth* (Brookfield Press, Queensland, 1992).
- S13. R. M. Wentzcovitch, B. B. Karki, M. Cococcioni, S. de Gironcoli, *Phys. Rev. Lett.* **92**, 018501 (2004).
- S14. R. M. Wentzcovitch, T. Tsuchiya, J. Tsuchiya, *Proc. Natl. Acad. Sci.* **103**, 543 (2006).
- S15. K. K. M. Lee *et al.*, *Earth Planet. Sci. Lett.* **223**, 381 (2004).
- S16. S. Stackhouse, J. P. Brodholt, J. Wookey, J. M. Kendall, G. D. Price, *Earth Planet. Sci. Lett.* **230**, 1 (2005).
- S17. A. K. McNamara, P. E. van Keken, S.-I. Karato, *Nature* **416**, 310 (2002).
- S18. M. Panning, B. Romanowicz, *Geophys. J. Int.* **167**, 361 (2006).
- S19. S.-i. Karato, S. Zhang, H.-R. Wenk, *Science* **270**, 458 (1995).
- S20. D. Yamazaki, S.-i. Karato, *Am. Mineral.* **86**, 385 (2001).
- S21. H. R. Wenk, S. Speziale, A. K. McNamara, E. J. Garnero, *Earth Planet. Sci. Lett.* **245**, 302 (2006).
- S22. S. Speziale, C. S. Zha, T. S. Duffy, R. J. Hemley, H. K. Mao, *J. Geophys. Res. B* **106**, 515 (2001).